Split-Vacancy Defect Complexes of Oxygen and Vacancies in hcp and fcc Cobalt

Shreyas Honrao, 1,2 Robert Maass,3 Dallas R. Trinkle,3 and Richard G. Hennig^{2,1,*}

¹Department of Materials Science and Engineering, Cornell University, Ithaca, New York 14853, U.S.A.

²Department of Materials Science and Engineering, University of Florida, Gainesville, Florida 32611, U.S.A.

³Department of Materials Science and Engineering, University of Illinois, Urbana-Champaign, Illinois 61801, U.S.A.

(Dated: August 1, 2020)

One of the most ubiquitous and important defects in solids is oxygen. Knowledge about the solubility and diffusivity of oxygen in materials is crucial to understand a number of important technological processes such as oxidation, corrosion, and heterogeneous catalysis. Density-functional theory calculations of the thermodynamics and kinetics of oxygen in cobalt show that oxygen diffusing into the two close-packed phases, α (hcp) and β (fcc), strongly interacts with vacancies. We observe the formation of oxygen split-vacancy centers (V-O_i-V) in both phases and show that this defect complex exhibits a similar migration energy barrier as the vacancy and oxygen interstitials. In contrast to the vacancy and oxygen interstitials, the oxygen split-vacancy centers exhibit an anisotropic strain field that couples to applied stress, making it possible to observe them through an internal friction experiment on quenched Co.

I. INTRODUCTION

Point defects in solids influence the mechanical, electronic, and optical properties of these materials. Often, small changes in defect chemistry can have a large effect on the way a material behaves. In transition metals oxides, for example, the parent compounds of the high-temperature cuprate superconductors are insulators; but the introduction of atomic point defects – either the removal of some oxygen ions or the substitution of some metal cations by others of different valence – is essential for the normal-state conductivity, from which superconductivity emerges [1].

Furthermore, these defects can move around. This results in atomic transport, which can play a significant role in the synthesis and processing of materials. In iron-copper alloys, vacancies are strongly bound to copper atoms, dragging them along to facilitate the precipitation of copper around vacancy sinks [2, 3]. Flux coupling can also result in the nucleation of thermodynamically unstable phases like Ni₃Si in undersaturated Ni(Si) alloys [4].

Some of the most interesting defect complexes involve the formation of a split-vacancy center (V-X_i-V), where two adjacent lattice sites are unoccupied, and a host or impurity atom occupies the interstitial position midway between the two vacant sites. The "semi-vacancy pair" (V-Si_i-V) [5] and "tin-vacancy pair" (V-Sn_i-V) [6] in silicon were the first experimentally observed *self* and *impurity* split-vacancy centers, respectively. Several *self* V-X_i-V's have been observed since in pyrochlores and other complex oxides [7, 8]. The known *impurity* V-X_i-V's however, are limited to metal impurity atoms in open diamond structures [9]. The formation of such *impurity* defect complexes has been attributed to the argument of strain relaxation of oversized impurities upon movement to the more spacious interstitial sites [9].

One of the most ubiquitous and important defects in solids is oxygen (O), which strongly reacts with most metals to form oxides. Many recent studies have shown that metal-oxygen

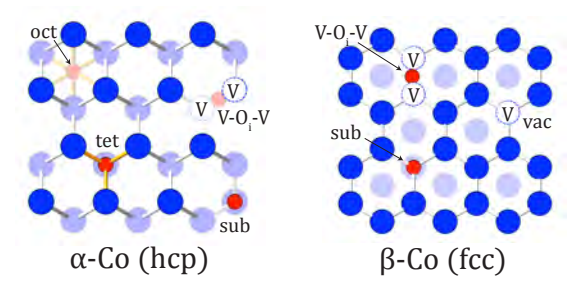


FIG. 1. (color online) Defects in α -Co (hcp) and β -Co (fcc) shown with the help of blue (cobalt), red (oxygen), and hollow (vacancy) circles. Depth fading is used to make atoms that lie further back to appear lighter.

systems exhibit a rich and complex surface phase space determined by pressure, temperature, and stoichiometry [10, 11]. Clearly, a precise knowledge of the detailed atomic structure of these systems is desired to improve our control of important technological processes like oxidation, corrosion, and heterogeneous catalysis, which involve interaction between metals and oxygen [12].

Cobalt (Co) and its oxides have recently received considerable attention for their applications in gas sensing, heterogeneous catalysis, intercalation compounds for energy storage, electrochromic devices, and as thermoelectric materials [13– 17]. Co has a rich phase diagram with three nearly degenerate crystal structures: α -Co (hcp), β -Co (fcc) and ϵ -Co (cubic) [18]. Under ambient conditions, cobalt crystallizes into α -Co [19]. On heating, the hcp phase transforms to the fcc β -Co structure at ~700 K, which is then stable all the way up to the melting temperature of ~ 1770 K [19]. The ϵ -Co phase possesses a more complex structure and its synthesis has only been possible through solution-phase chemistry processes [20, 21]. All three phases are ferromagnetic; however, a Curie temperature ($T_c = 1388 \text{ K}$) has been defined only for the fcc β -Co phase [19] since both α -Co and ϵ -Co transform to the fcc phase before achieving a paramagnetic structure.

Even though we have detailed knowledge about the structure, properties, and processing of different Co phases, very

^{*} rhennig@ufl.edu

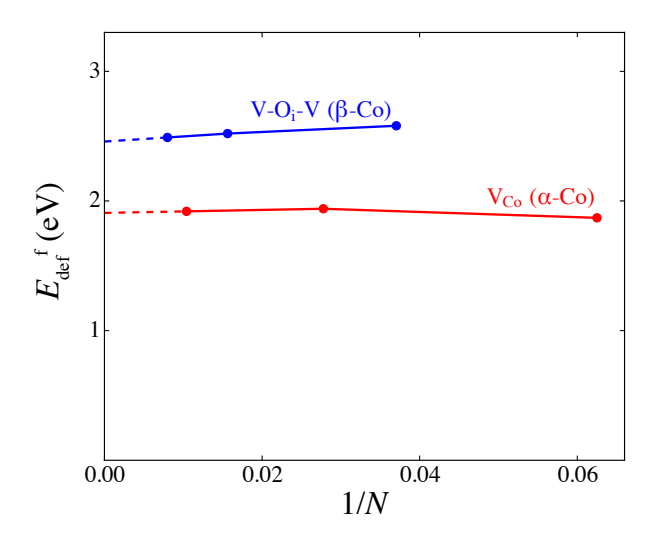


FIG. 2. (color online) Finite-size effects on the defect formation energies ($E_{\rm def}^{\rm f}$) in cobalt. We find that $E_{\rm def}^{\rm f}$ is accurate to within 0.03 eV for larger supercells.

little is known about the thermodynamics and kinetics of O in Co. In this work, we use density-functional theory (DFT) to show that both close-packed phases of Co display complex defect structures in the presence of O, affecting the transport of O as well as of vacancies (V) in Co. We first predict the equilibrium point defect structures for O, V, and their complexes in α -Co and β -Co and then determine how these defects migrate through the crystal structures. We show that O has a high solubility and diffusivity as an interstitial (O_i). Surprisingly, however, Oi strongly reacts with V to form split-vacancy centers (V-O_i-V), which provide an alternate pathway for O and V diffusion in Co. We show that these V-O_i-Vs exhibit an anisotropic strain field that couples to applied stress, in contrast to the isotropic strain fields of the V and O_i defects. This leads to a behavior similar to the observed Snoek effect for carbon and nitrogen in bcc Fe [22] and allows for the experimental detection of these complexes by internal friction measurements.

II. METHODS

We perform the DFT calculations with the projector augmented wave method [23, 24] as implemented in the VASP code [25–28] using the gradient-corrected PBE exchange-correlation functional [29]. Calculations are carried out with periodic boundary conditions, with wave functions expanded on a plane-wave basis set. The energy cutoff and the corresponding cutoff for the augmentation functions are set to 400 eV and 650 eV respectively to ensure convergence of the total energy to within 1 meV/atom. The *k*-point integration of the Brillouin zone is performed using Monkhorst and Pack meshes [30] with a density of 30 k-points per inverse Ångstrom. We use spin-polarization to account for the magnetism in these materials. We also constrain the cell shape and volume to be constant for all our calculations.

TABLE I. Finite-size effects on the defect formation energies ($E_{\rm def}^{\rm f}$) in cobalt. We find that $E_{\rm def}^{\rm f}$ is accurate to within 0.03 eV for larger supercells.

Defect	Structure	Supercell size	$N_{ m atoms}$	$E_{\mathrm{def}}^{\mathrm{f}}[\mathrm{eV}]$
V_{Co}	α (hcp)	$2 \times 2 \times 2$	16	1.87
		$3 \times 3 \times 2$	36	1.94
		$4 \times 4 \times 3$	96	1.92
$V-O_i-V$	β (fcc)	$3 \times 3 \times 3$	27	2.58
		$4 \times 4 \times 4$	64	2.52
		$5 \times 5 \times 5$	125	2.49

TABLE II. Defect formation energies $(E_{\rm def}^{\rm f})$ in cobalt. Interstitial atoms in hcp and fcc can occupy either the octahedral or tetrahedral sites. Both energies $(E_{\rm oct}, E_{\rm tet})$ are reported.

Defect	α-Co (hcp)	β-Co (fcc)
$\overline{V_{Co}}$	1.92	1.79
O_{Co}	1.84	1.92
$O_{Co} + V_{Co}$	2.51	2.49
Oi	0.52, 1.28	0.49, 1.25
Co _i	5.19, 4.49	4.48, —

For a defect-mediated diffusion mechanism, the activation energy of diffusion, $E_{\rm def}^{\rm act}$, is given by the sum of the defect formation energy, $E_{\rm def}^{\rm f}$, and the defect migration energy barrier, $E_{\rm def}^{\rm m}$. We calculate the migration barriers with the climbing image nudged elastic band (NEB) method [31, 32] using 1-3 intermediate images to describe the transition pathways between neighboring lattice and interstitial defect sites. We look at simple paths as well as more complex ones involving a concerted movement of multiple species. Comparing the total activation energies for competing mechanisms helps us determine the dominant diffusion processes controlling the kinetics in these systems.

III. FINITE SIZE ERROR OF DEFECT ENERGIES

The formation energies of defects in DFT calculations that employ periodic boundary conditions are affected by the size of the unit cell. Table I and Fig. 2 compare the effects of varying cell size on defect formation energies. To reduce finite-size effects, we choose our unit cells to be as large as possible while being computationally feasible. We use a $4\times4\times3$ supercell (96 atoms) of α -Co and a $5\times5\times5$ supercell (125 atoms) of β -Co for all our calculations, which provide defect formation energies accurate to within 0.03 eV.

IV. DEFECT STABILITY

To determine the stability of point defects in Co, we calculate formation energies for: (i) vacancy on a cobalt site (V_{Co}) , (ii) substitutional oxygen atom on a cobalt site (O_{Co}) ,

TABLE III. Binding energies (in eV) of the oxygen-vacancy complex in α -Co and β -Co for first (1NN), second (2NN) and third nearest neighbor (3NN) sites relative to the isolated defects. The symmetric V-O_i-V configuration is observed to be the most stable one for 1NN and 2NN sites in both α -Co and β -Co.

	1NN	2NN	3NN
α-Co	1.25	1.14	0.68
β -Co	1.22	1.32	0.68

(iii) substitutional oxygen atom and a neighboring vacancy $(O_{Co}+V_{Co})$, (iv) oxygen atom on an interstitial site (O_i) , and (v) cobalt atom on an interstitial site (Co_i) . We use the chemical potential of oxygen in rocksalt CoO as reference. Table II compares the formation energies for the various defects in α -Co and β -Co. We don't report an energy for the tetrahedral Co_i defect in β -Co as it always relaxes into an octahedral position.

We make an interesting observation for the case of a substitutional O atom sitting next to a vacancy in β -Co: the $O_{Co}+V_{Co}$ defect complex relaxes to form a highly stable V-O_i-V split-vacancy center with the O atom occupying the interstitial space between two vacancies. This is similar to the tin split-vacancy center (V-Sn_i-V) in silicon studied by Watkins et al. [6]. We also see the same defect occur in α -Co; however, the formation of V-O_i-V in the hcp phase is limited to the case where the two neighboring vacancies lie in separate basal planes. If the neighboring vacancies occupy positions in the same basal plane, the O atom no longer relaxes to a symmetric center position.

To search for other split-vacancy centers, we extend our calculations to include the $O_{Co}+V_{Co}$ defect with V and O as 2nd and 3rd nearest neighbors to each other (2NN and 3NN). We observe the formation of V-O_i-V in the 2NN case but not 3NN, for both α -Co and β -Co.

Table III shows the strong binding energies for the split-vacancy O defect in the 1NN and 2NN configurations in α -Co and β -Co. Even in the 3NN case, where a split-vacancy center does not form, we still see significant binding between the O and V. We define the binding energy as the difference in energies between a system with interacting defects and a system with isolated defects far away from each other. A large positive binding energy implies there is a strong attraction between the individual defects. We find that the binding is equally strong in the 1NN and 2NN configurations but gets weaker as the individual defects move further apart from each other (3NN).

As stated earlier, previous research showed the occurence of *impurity* split-vacancy centers being limited to open diamond structures thus far, where a large metal impurity atom (M) relaxed to occupy the more spacious position between two neighboring vacancies (V-M_i-V). The reason for the formation of such complexes was not completely understood. The argument of strain relaxation of oversized impurities that was proposed to explain the formation of the Sn-V complex in Si [9] does not fit our description of a smaller O atom forming

a similar complex in close-packed Co. While strain probably play a role, we believe there might also be other factors at play. On closer examination we see that O sits on a distorted octahedral site in the V-O_i-V configuration, albeit with two missing Co neighbors. This resembles the geometry and coordination it has in the rocksalt CoO phase that would form with sufficient O present. The Co-O distance in the V-O_i-V configuration is found to be 2.0 Å, which is intermediate between the Co-O distances in the interstitial and substitutional configuration of 1.9 and 2.5 Å, and closer to the value for CoO of 2.1 Å. This suggests that strain coupled with the natural tendency of the impurity O atoms to stabilize into a CoO-like local configuration might explain the formation of these O split-vacancy centers in Co.

V. DEFECT REACTIONS AND MIGRATION

Next, we calculate migration barriers for Co and O atoms diffusing from one defect site to another, to infer the most likely mechanism for diffusion in α -Co and β -Co. We identify mechanisms of diffusion for Co through vacancies, and for O through vacancies and interstitial sites. Table IV lists the formation energies, migration barriers and total activation energies for the various defects in Co. We find that the migration barriers for diffusion through the two close-packed phases are surprisingly similar for V_{Co} , O_i , and V- O_i -V. For the oxygen interstitial, we find that the octahedral–tetrahedral–octahedral interstitial path exhibits the lowest migration energy barrier. Figures 3 and 4 illustrate the diffusion pathways of the 1NN V- O_i -V defect through other 1NN V- O_i -V and 2NN V- O_i -V sites.

Finally, we combine the defect formation energies with knowledge of the migration barriers to obtain a complete picture of the diffusion of O in Co (Table IV). The formation energies indicate that O prefers to sit on the O_i sites in Co. Not only does O have the highest solubility on such sites, but it also has a small migration barrier to move between them, providing what appears to be the fastest mechanism for O diffusion in Co. If such an O_i were to encounter a V_{Co} , however, they can exothermally combine to form O_{Co} ,

$$O_i + V_{Co} \rightleftharpoons O_{Co}$$
. (1)

The reaction energies are -0.60 and -0.36 eV in α -Co and β -Co, respectively. This substitutional O_{Co} can only move when it encounters another V_{Co} , at which point they combine exothermally to form the V-O_i-V split-vacancy center,

$$O_{Co} + V_{Co} \rightleftharpoons V - O_i - V,$$
 (2)

with a reaction energy of -1.25 and -1.22 eV in $\alpha\text{-Co}$ and $\beta\text{-Co}$, respectively. Table IV shows that the migration barriers for V-O_i-V are similar to the barriers for O_i and V_{Co}, suggesting that the formation of V-O_i-V complexes does not trap oxygen and vacancies, and that V-O_i-V diffusion could provide an alternate mechanism for O and Co transport through close-packed Co.

To experimentally detect the presence of V-O_i-V complexes requires that they form in sufficient concentrations, which will

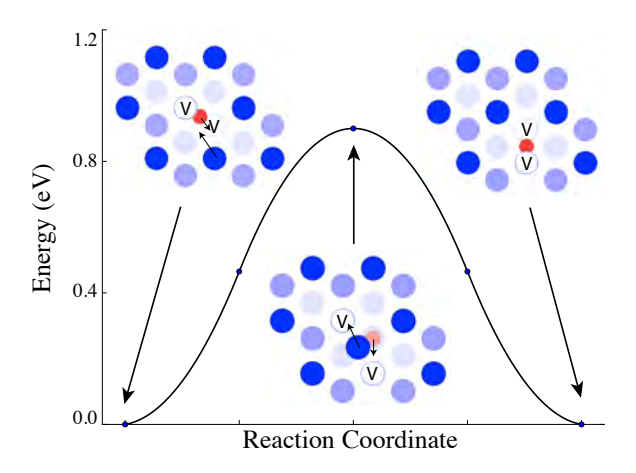


FIG. 3. (color online) Diffusion between two neighboring 1NN oxygen split-vacancy centers (V-O_i-V) is shown for β -Co (fcc). This mechanism involves a concerted motion of Co and O atoms.

TABLE IV. Diffusion activation energies for the various defects in Co. The considered mechanisms include Co diffusing through vacancies (V_{Co}) : $Co_{Co}+V_{Co}\rightarrow V_{Co}+Co_{Co}$; O diffusing through interstitials (O_i) : $O_i^{oct}\rightarrow O_i^{tet}\rightarrow O_i^{oct}$; 1NN V-O_i-V defect diffusing to 1NN V-O_i-V sites (1NN): V-O_i-V^{1NN} \rightarrow V-O_i-V^{1NN} and 1NN V-O_i-V defect diffusing to 2NN V-O_i-V sites (2NN): V-O_i-V^{1NN} \rightarrow V-O_i-V^{2NN}.

D.a	α-Co (hcp)	β-Co (fcc)	
Diffusion	$E_{ m def}^{ m f} \ E_{ m def}^{ m m} \ E_{ m def}^{ m act}$	$E_{ m def}^{ m f}$ $E_{ m def}^{ m m}$ $E_{ m def}^{ m act}$	
V_{Co}	1.92 0.86 2.78	1.79 1.00 2.79	
O_i	0.52 0.91 1.43	0.49 0.99 1.48	
$V-O_i-V$ (1NN)	2.51 0.90 3.41	2.49 0.91 3.40	
V - O_i - V (2NN)	2.51 1.31 3.82	2.49 1.38 3.87	

depend on the processing of the material. To determine the equilibrium concentration of the V-O_i-V defects, we obtain the equilibrium constant for the combined reaction of Eqs. (1) and (2),

$$O_{Co} + 2V_{Co} \rightleftharpoons V - O_i - V$$
 (3)

$$O_{\text{Co}} + 2V_{\text{Co}} \rightleftharpoons V - O_{\text{i}} - V$$

$$K_{\text{eq}} = \exp\left(-\frac{\Delta E}{kT}\right) = \frac{[V - O_{\text{i}} - V]}{[O_{\text{i}}][V_{\text{Co}}]^2}.$$
(4)

The concentration of V-O_i-V is clearly limited by the total number of V_{Co} in our system, since two vacancies are needed to form every split-vacancy center. Using the vacancy formation energy for β -Co, we estimate the room temperature equilibrium concentration of vacancies, $[V_{Co}] = 9 \times 10^{-31}$, implying a negligibly small concentration of V-O_i-V.

The vacancy concentration in a material can generally be increased by quenching from high temperature or by irradiation. A quench from 1700 K, just below the melting point of 1770 K, to 700 K increases [V_{Co}] in β -Co to 5 × 10⁻⁶. Assuming the quenched vacancy concentration and the oxygen concentration of 1×10^{-3} are fixed in the bulk of the sample away from any sources or sinks, we calculate the equilibrium

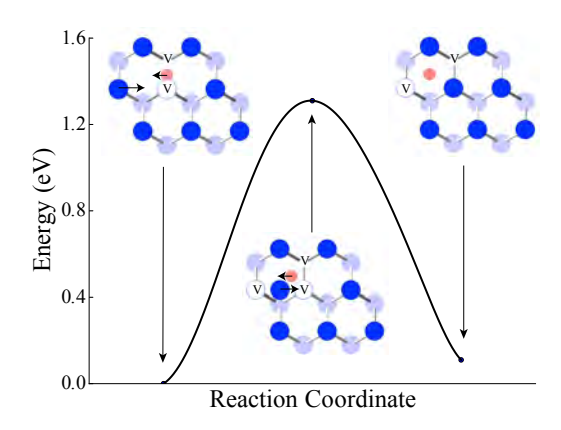


FIG. 4. (color online) Diffusion between a 1NN and 2NN oxygen split-vacancy center (V-O_i-V) is shown for α -Co (hcp). This mechanism involves a concerted motion of Co and O atoms.

concentration of V-O_i-V at 700 K to be 2.45×10^{-6} . This result, that at intermediate temperatures essentially all vacancies are bound in the form of the V-O_i-V complexes, is a direct consequence of the significantly higher reaction energy of the reaction in Eq. (2).

In order for V-O_i-V to form, the O_i and V_{Co} must also encounter each other fairly quickly. For $[V_{Co}] = 5 \times 10^{-6}$, we estimate the time scale for the encounters at 700 K to be of a few ms according to

$$\langle R_n^2 \rangle = nr^2 = t\Gamma r^2 = 6Dt, \tag{5}$$

where $\langle R_n^2 \rangle$ is the mean square displacement after time t, n is the number of jumps, r is the individual jump length, Γ is the jump frequency and D is the diffusion coefficient. This time scale is sufficiently short to convert all V_{Co} into V-O_i-V split-vacancy centers during the quench while avoiding thermal equilibration of the vacancy concentration at grain boundaries and interfaces. We conclude that as long as there is a sufficient number of quenched V_{Co}, and mobile O_i encounter the V_{Co}, V-O_i-V will form even against the observed formation energy trend in Table II.

VI. INTERNAL FRICTION

The experimental assessment of damping mechanism in metals has a long history [33], where cross-comparisons between different reported damping mechanisms is not always easy since each particular measurement technique is limited to a given frequency range. Consequently, most experiments have been done in different frequency regimes and over a range of temperatures that is either above or below room temperature.

In the particular case of damping due to interstitials, considerable efforts have been dedicated to studying hydrogen (H), oxygen (O), or nitrogen (N) in bcc lattices [34, 35], whereas hcp lattices, and in particular Co, have been less commonly investigated. However, a series of earlier studies using the

torsion pendulum method, often operated at frequencies at or close to 1 Hz, were dedicated to interstitial sites relaxation processes in hcp crystals [36–40]. This body of experimental work reports mechanical relaxation that occurs in the range of 700–750 K, depending on the metal (Ti, Hf, Zr). This temperature range overlaps with the allotropic phase transition from α -Co to β -Co and may be the main reason for the lack of experimental evidence of Snoek-type losses.

In the case of Ti. Pratt et al. reported that the purest polycrystalline grade only exhibits an internal friction signature from grain-boundary processes [36], whereas the careful introduction of 1.5-4.5 at% O revealed a relaxation peak at ~700 K, the magnitude of which was proportional to the Ocontent. Qualitatively, the same was reported for reactorgrade Hf (containing 6 wt% Zr) by Bisogni et al. [38], where the loss process is seen at ~750 K and a frequency of 0.9 Hz. These experimental observations were in contrast to the conclusion that losses of Snoek type ought not to be seen for interstitials in fcc or hcp due to the geometry of the octahedral and tetrahedral site [38], where O is expected to occupy the former because of its atomic size. Gupta and Weinig convincingly addressed this discrepancy experimentally by demonstrating that substitutional impurities are the cause for the observed damping. Due to the local lattice distortion caused by the substitutional element, the relaxation of interstitial-solute (i-s) pair was consequently shown to depend on the relative atomic size mismatch between the base element and the solute and scale with solute concentration at constant O-content [37]. Interstitial-interstitial (i-i) pair relaxation had been theoretically predicted [41], and was subsequently shown for dilute Ti-, Hf-, and Zr-alloys [40] in the aforementioned temperature range. These experimental efforts have in common that they use low-frequency excitations and study a temperature regime from room temperature to ~875 K and are limited to Ti, Hf, and Zr.

With a view to experimentally confirm the presence of V-O_i-V and study its diffusion, we determine how the defect couples to applied stress in β -Co. The V-O_i-V complexes in β -Co are oriented along any of the $\langle 110 \rangle$ directions, producing six different orientations ([110] and [$\bar{1}\bar{1}0$] are identical). The derivative of the defect energy with respect to strain is the elastic dipole tensor, \underline{P} . For the case of a V-O_i-V defect oriented along the [110] direction, we find

$$\underline{P} = \begin{pmatrix} -2.70 & 0.13 & 0\\ 0.13 & -2.70 & 0\\ 0 & 0 & -4.30 \end{pmatrix} \text{ GPa.}$$
 (6)

This dipole tensor indicates an anisotropic compression of the structure. The compression is expected for a defect involving two vacancies. The anisotropy of the dipole tensor is a necessary ingredient for internal friction loss due to an oscillating applied stress. The largest coupling to applied stress is due to the difference between the "in-plane" (–2.70 GPa) normal component and the "out-of-plane" (–4.30 GPa) normal component, which can couple to either uniaxial or shear stresses differently for each of the twelve (110) V-O_i-V complexes. The in-plane shear component (0.13 GPa) is an order of magnitude smaller and plays a negligible role in internal

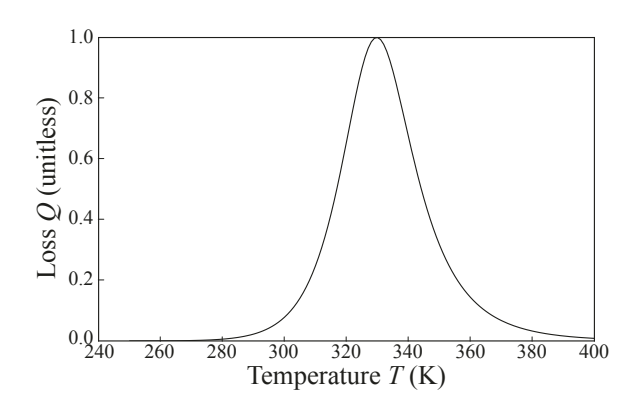


FIG. 5. Predicted internal friction loss per cycle at $\nu=1$ Hz due to V-O_i-V complexes in β -Co. Under a cyclic non-hydrostatic load, the lowered symmetry of the complexes produces different changes in energy for different sites; this drives transitions from higher to lower energy states, producing loss in energy, similar to the Snoek effect from C in bcc-Fe. The loss is proportional to the concentration of V-O_i-V, and reaches a peak near 330K.

friction. Appendix A provides a detailed derivation of the loss due to internal friction. The loss Q^{-1} depends on the jump rate $\lambda = \nu_0 \exp(-E_{\rm def}^{\rm m}/k_{\rm B}T)$, where $E_{\rm def}^{\rm m} = 0.91$ eV (Table IV); only one eigenvalue of the transition matrix couples strongly to shear strains, so

$$Q^{-1} \propto \frac{[\text{V-O}_{\text{i}}\text{-V}]}{k_{\text{B}}T} \frac{12\lambda\nu}{\nu^2 + (12\lambda)^2},$$
 (7)

which is plotted in Figure 5. The prediction for internal friction shows that for a torsional pendulum of a quenched Co wire with $\nu = 1$ Hz, the peak loss Q^{-1} corresponding to maximum damping should occur near 330K.

Snoek-type relaxations in Co remain experimentally unexplored, but the consistently observed features for other hcp metals suggest that similar i-s and i-i mechanisms could occur in Co. It is worth noting that torsion pendulum data recorded when studying the hcp-fcc transition at 0.5 Hz in Co displays at least one unexplored small peak at ~550 K both during cooling and heating [42]. The here theoretically predicted room-temperature loss mechanism was not identified in any of the studied hcp metals, which may find its origin in the continuously increasing damping with temperature that will drown small amplitude peaks at the low temperature end. Additional experimental efforts that carefully examine low-frequency excitations at and around room temperature are thus critically needed as to test our predictions and to potentially identify a loss mechanism that is generic to hcp lattices that contain solved O.

VII. CONCLUSION

To conclude, we performed DFT calculations to measure the formation energies and migration barriers of O point defects in α (hcp) and β (fcc) cobalt. We predict that in both phases O strongly interacts with vacancies to form oxygen split-vacancy centers V-O_i-V in the presence of sufficiently

high vacancy concentrations. We show that the oxygen split-vacancy centers do not trap oyxgen and provide an alternate mechanism for oxygen diffusion in close-packed cobalt. We propose a way to observe and measure their diffusion through an internal friction experiment. We show that the oxygen split-vacancy centers exhibit an anisotropic strain field, in contrast to the isolated vacancies and oxygen interstitials. This strain field couples to applied stress and the diffusion of V-O_i-V leads to a maximum damping in internal friction at experimentally accessible frequencies and temperatures. Similar split-vacancy centers may also occur for oxygen and other interstitial species in various close-packed materials.

ACKNOWLEDGMENTS

This work was supported by the NSF under the awards Nos. ACI-1440547 and CHE-1665310. This research used computational resources provided by the University of Florida Research Computing (http://researchcomputing.ufl.edu) and the Texas Advanced Computing Center under Contracts TG-DMR050028N, TG-DMR140143, and TG-DMR150006. This work used the Extreme Science and Engineering Discovery Environment (XSEDE), which is supported by National Science Foundation grant number ACI-1053575.

Appendix A: Loss under cyclic loading

1. Definitions

To consider the energy loss per cycle under mechanical load due to transitions between defect sites, we use the nomenclature introduced for the derivation of transport coefficients for interstitial defects [43]. We have a set of N defects in our unit cell that can be indexed using i = 1...N, and where a series of possible transitions between these defects are possible. For a defect state i in the unit cell, it has an equilibrium site probability ρ_i that follows the Arrhenius relationship,

$$\rho_i := cZ^{-1}\rho_i^0 \exp\left(-\beta E_i\right) \tag{A1}$$

for site energy E_i , concentration per unit cell c, entropic prefactor $\rho_i^0 = \exp(S_i/k_{\rm B})$, and partition function $Z = \sum_i \rho_i^0 \exp(-\beta E_i)$. The transition from site i to site j has a rate $\lambda_{i \to i}$,

$$\lambda_{i \to j} := \frac{\lambda_{ij}^{0}}{\rho_{\cdot}^{0}} \exp\left(-\beta \left[E_{ij}^{\text{ts}} - E_{i}\right]\right) \tag{A2}$$

for transition state energy $E^{\rm ts}_{ij}$ and entropic prefactor $\lambda^0_{ij} = \exp(S^{\rm ts}_{ij}/k_{\rm B})$, following [44]. In this formulation, the transition state energy and entropic prefactors are equal for $i \to j$ and for $j \to i$, while it is not necessary that $\lambda_{i \to j}$ and $\lambda_{j \to i}$ are equal. Finally, the probabilities obey detailed balance, where $\rho_i \lambda_{i \to j} = \rho_j \lambda_{j \to i}$ for all i, j.

We will assume that the stress amplitude is sufficiently small that we are in a linear elastic regime, there is a small defect concentration, and that the energy loss is a small perturbation in the system energy. The dilute limit permits us to ignore defect-defect interactions. The linear elastic limit allows us to transform from a stress amplitude into a strain amplitude, and to the write the changes to our site probabilities and transition rates to first order in the strain using the elastic dipole. The elastic dipole tensor \underline{P}_i for a site i is

$$\underline{P}_i := -\frac{dE_i}{d\varepsilon}.$$
 (A3)

The elastic dipole can be conveniently evaluated in a supercell calculation from the stress in the cell: an interstitial is added to an initially undefected, unstressed supercell containing N atoms (with equilibrium volume V_0 per atom), resulting in a stress $\underline{\sigma}$, then to first order in N^{-1} ,

$$P \approx NV_0\sigma$$
, (A4)

which is straightforward to evaluate with density-functional theory methods; e.g., see [45–48]. Similarly, the energy of a transition state can also change with strain, as dictated by the elastic dipole tensor for the transition state \underline{P}_{ij}^{ts} for the transition state between i and j,

$$\underline{P}_{ij}^{\text{ts}} := -\frac{dE_{ij}^{\text{ts}}}{d\varepsilon}.$$
 (A5)

This, too, can be approximated by the stress at the transition state in a supercell calculation as in Eqn. A4; e.g., see [47, 49]. The definitions of elastic dipoles allow the introduction of a small strain perturbation $\delta\underline{\varepsilon}$ to produce site energies changes δE_i and transition energies δE_{ij}^{ts} as

$$\delta E_i = -\underline{P}_i : \delta \underline{\varepsilon}$$

$$\delta E_{ii}^{ts} = -\underline{P}_{ii}^{ts} : \delta \underline{\varepsilon}$$
(A6)

which is correct to first order in strain.

2. Master equation

The evolution of the defects is defined by the Master equation, and we can include the effect of a (perturbative) time-dependent strain. The time-dependent occupancy $c_i(t)$ of site i is given by

$$\frac{dc_i}{dt} = \sum_j \lambda_{j\to i} c_j(t) - \lambda_{i\to j} c_i(t). \tag{A7}$$

We introduce the rate matrix Λ_{ii} ,

$$\Lambda_{ij} := \begin{cases} \lambda_{i \to j} & : i \neq j \\ -\sum_{j} \lambda_{i \to j} & : i = j \end{cases}$$
 (A8)

and so Eqn. A7 is simply $\dot{c}=c\Lambda$. By detailed balance, the equilibrium site probability ρ satisfies $\rho\Lambda=0$. Similar to our

expressions for changes in site and transition energies, a small strain introduces a change in the rate matrix $\delta \Lambda_{ij}$: $\delta \varepsilon$

$$\delta\Lambda_{ij}: \delta\underline{\varepsilon} := \begin{cases} \lambda_{i \to j} (k_{\rm B}T)^{-1} (\underline{P}_{ij}^{\rm ts} - \underline{P}_{i}) : \delta\underline{\varepsilon} & : i \neq j \\ -\sum_{j} \lambda_{i \to j} (k_{\rm B}T)^{-1} (\underline{P}_{ij}^{\rm ts} - \underline{P}_{i}) : \delta\underline{\varepsilon} & : i = j \end{cases}$$
(A9)

based on Eqn. A2. If we consider that our system is close to equilibrium, so that

$$c_i(t) = \rho_i + \underline{F}_i : \delta \underline{\varepsilon}(t),$$
 (A10)

then the (time-dependent) Master equation in the perturbative limit is

$$\underline{F}_{i} : \delta \underline{\varepsilon}(t) = \sum_{j} (\rho_{j} + \underline{F}_{j} : \delta \underline{\varepsilon}(t))(\Lambda_{ji} + \delta \Lambda_{ji} : \delta \underline{\varepsilon}(t))$$

$$= \sum_{j} (\underline{F}_{j} \Lambda_{ji}) : \delta \underline{\varepsilon}(t) + \sum_{j} \rho_{j} \delta \Lambda_{ji} : \delta \underline{\varepsilon}(t) + O(\delta \underline{\varepsilon}^{2})$$
(A11)

This can be solved for a cyclic strain $\delta \underline{\varepsilon}(t) = \delta \underline{\varepsilon}_0 e^{i\nu t}$ with frequency ν , so that $\dot{\delta \varepsilon}(t) = i\nu \delta \varepsilon(t)$, and we have

$$\sum_{j} \underline{F}_{j} (i\nu \delta_{ji} - \Lambda_{ji}) = \sum_{j} \rho_{j} \delta \Lambda_{ji}$$

$$\underline{F}_{i} = \sum_{ik} \rho_{j} \delta \Lambda_{jk} (i\nu \mathbf{1} - \Lambda)_{ki}^{-1}$$
(A12)

The first term in the sum, $\sum_{i} \rho_{i} \delta \Lambda_{jk}$, simplifies as

$$\sum_{j} \rho_{j} \delta \Lambda_{jk} = \sum_{j} \rho_{j} \lambda_{j \to k} (k_{\rm B}T)^{-1} (\underline{P}_{jk}^{\rm ts} - \underline{P}_{j})$$

$$- \sum_{j} \rho_{k} \lambda_{k \to j} (k_{\rm B}T)^{-1} (\underline{P}_{kj}^{\rm ts} - \underline{P}_{k})$$

$$= (k_{\rm B}T)^{-1} \sum_{j} \rho_{j} \lambda_{j \to k} \left[\underline{P}_{jk}^{\rm ts} - \underline{P}_{j} - \underline{P}_{kj}^{\rm ts} + \underline{P}_{k} \right]$$

$$= - (k_{\rm B}T)^{-1} \sum_{j} \rho_{j} \underline{P}_{j} \Lambda_{jk}$$
(A13)

so that Eqn. A12 becomes

$$\underline{F}_{i} = -(k_{\rm B}T)^{-1} \sum_{jk} \rho_{j} \underline{P}_{j} \Lambda_{jk} (i\nu \mathbf{1} - \Lambda)_{ki}^{-1}$$
(A14)

To compute the loss per cycle, we integrate the time derivative of the energy multiplied by the instantaneous occupancy of each site over one cycle. The time derivative of energy is the work done on each defect, which is at the expense of the elastic energy in the system. The instantaneous energy of each site is $E_i(t) = \Re(E_i - \underline{P}_i : \delta\underline{\varepsilon}_0 e^{i\nu t})$, while $c_i(t) = \Re(\rho_i + \underline{F}_i : \delta\underline{\varepsilon}_0 e^{i\nu t})$, and so

$$-\sum_{i} c_{i}(t)\dot{E}_{i}(t) = -\sum_{i} \left(\rho_{i} + \Re \underline{F}_{i} : \delta \underline{\varepsilon}_{0} \cos(\nu t) - \Im \underline{F}_{i} : \delta \underline{\varepsilon}_{0} \sin(\nu t)\right) \left(\nu \underline{P}_{i} : \delta \underline{\varepsilon}_{0} \sin(\nu t)\right)$$
(A15)

We integrate the change in energy over one cycle to find

$$\Delta E_{\text{cycle}} = -\int_{0}^{2\pi v^{-1}} dt \sum_{i} c_{i}(t) \dot{E}_{i}(t)$$

$$= \int_{0}^{2\pi v^{-1}} dt \sum_{i} \left[\left(\underline{P}_{i} : \delta \underline{\varepsilon}_{0} \right) \left(\Im \underline{F}_{i} : \delta \underline{\varepsilon}_{0} \right) v \sin^{2}(vt) \right]$$

$$= \pi \sum_{i} \left(\delta \underline{\varepsilon}_{0} : \underline{P}_{i} \right) \left(\Im \underline{F}_{i} : \delta \underline{\varepsilon}_{0} \right)$$
(A16)

To convert this to a fractional loss per cycle, we need to divide by the *elastic* energy per cycle, which is $\pi\Omega_0\delta\underline{\varepsilon}_0$: \underline{C} : $\delta\underline{\varepsilon}_0$, for the elastic constant tensor C and volume per unit cell Ω_0 .

We can find the solution for the loss by eigendecomposing the matrix Λ , and rewriting Eqn. A14 and Eqn. A16 in terms of its eigenvectors and values. While the matrix Λ is generally not symmetric, the matrix

$$\omega_{ij} := \rho_i^{1/2} \Lambda_{ij} \rho_i^{-1/2} \tag{A17}$$

is. Moreover, it is a negative semidefinite matrix, with exactly one zero eigenvalue; let r^n be the real, negative eigenvalues where $r^0=0$, and s^n the corresponding eigenvectors, where $s_i^0=\rho_i^{1/2}$. As $\Lambda_{ij}=\rho_i^{-1/2}\omega_{ij}\rho_j^{1/2}$, it follows that

$$\sum_{k} \Lambda_{jk} (i\nu \mathbf{1} - \Lambda)_{ki}^{-1} = \sum_{n} \frac{r^{n}}{i\nu - r^{n}} \rho_{j}^{-1/2} s_{j}^{n} s_{i}^{n} \rho_{i}^{1/2}.$$
 (A18)

We note that

$$\Im \frac{r^n}{i\nu - r^n} = -\frac{\nu r^n}{\nu^2 + (r^n)^2}$$
 (A19)

and so the fourth-rank tensor in Eqn. A16 is

$$\underline{\mathcal{L}}(\nu, T) := \sum_{i} \underline{P}_{i} \otimes \Im \underline{F}_{i}$$

$$= (k_{\rm B}T)^{-1} \sum_{n>0} \frac{\nu r^{n}}{\nu^{2} + (r^{n})^{2}} \left(\sum_{i} \rho_{i}^{1/2} s_{i}^{n} \underline{P}_{i} \right) \otimes \left(\sum_{i} \rho_{i}^{1/2} s_{i}^{n} \underline{P}_{i} \right), \tag{A20}$$

which is symmetric and negative definite, as $r^n < 0$ for all n > 0, and hence the loss-per-cycle Q^{-1} is

$$Q^{-1} = -\frac{\delta \underline{\varepsilon}_0 : \underline{\mathcal{L}}(\nu, T) : \delta \underline{\varepsilon}_0}{\Omega_0 \delta \underline{\varepsilon}_0 : \underline{C} : \delta \underline{\varepsilon}_0}.$$
 (A21)

Note that the temperature dependence appears explicitly in Eqn. A20 and in the temperature dependence of the rates in Λ , and hence r^n and s^n . There is a linear dependence in concentration c from the linear dependence of ρ_i in Eqn. A20.

3. Isotropic representation

The fourth-rank loss tensor $\underline{\mathcal{L}}$ can be simplified by converting to rotationally averaged scalar quantities: bulk \mathcal{L}^b , shear

 \mathcal{L}' , and uniaxial \mathcal{L}^u corresponding to bulk, shear, or uniaxial strains in a random polycrystal,

$$\mathcal{L}^{b} = \frac{1}{9} \left\{ \mathcal{L}_{1111} + \mathcal{L}_{2222} + \mathcal{L}_{3333} + 2\mathcal{L}_{1122} + 2\mathcal{L}_{1133} + 2\mathcal{L}_{2233} \right\}$$

$$\mathcal{L}' = \frac{1}{5} \left\{ \frac{1}{3} \left(\mathcal{L}_{1111} + \mathcal{L}_{2222} + \mathcal{L}_{3333} - \mathcal{L}_{1122} - \mathcal{L}_{1133} - \mathcal{L}_{2233} \right) + \right.$$

$$\left. + \mathcal{L}_{1212} + \mathcal{L}_{1313} + \mathcal{L}_{2323} \right\}$$

$$\mathcal{L}^{u} = \mathcal{L}^{b} + \frac{4}{3} \mathcal{L}'$$
(A22)

For the case of loss per cycle in a torsion pendulum, \mathcal{L}' is the quantity of interest.

4. Loss for oxygen-vacancy complexes in FCC cobalt

For the case of the FCC Co oxygen-vacancy complex, the loss calculation simplifies to two eigenmodes. We can identify an oxygen-vacancy complex in an FCC material based on the positions of the oxygen atom alone, as the two neighboring vacancy positions are unique. Crystallographically, this is similar to the "crowdion" interstitial defect. In the space group of FCC $(Fm\bar{3}m)$, these are the d sites, of which there are six as many compared with the a sites for the solvent atoms. These sites, in Cartesian coordinates, are:

In the primitive unit cell, we only need one entry from each row, as each row represent the same *orientation*: [011], $[0\bar{1}1]$, [101], $[10\bar{1}]$, [110], and $[\bar{1}10]$. As all of the sites have the

same energy, and hence $\rho=c$. From any site, there are eight jumps that all have the same rate, λ ; the transitions involve moving one of the two vacancies to a neighboring site *that is also a neighbor of the other vacancy* while it remains in place. This is equivalent to the oxygen atom displacing by $\langle \frac{1}{4} \frac{1}{4} 0 \rangle$; however, only eight jumps are possible for each orientation. The transition rate matrix is

$$\Lambda = \omega = \lambda \begin{pmatrix} -8 & 0 & 2 & 2 & 2 & 2 \\ 0 & -8 & 2 & 2 & 2 & 2 \\ 2 & 2 & -8 & 0 & 2 & 2 \\ 2 & 2 & 0 & -8 & 2 & 2 \\ 2 & 2 & 2 & 2 & -8 & 0 \\ 2 & 2 & 2 & 2 & 0 & -8 \end{pmatrix}$$
(A24)

The elastic dipole for a site with orientation [110] is

$$\underline{P}_{[110]} = \begin{pmatrix} P^{\parallel} & P^{s} & 0 \\ P^{s} & P^{\parallel} & 0 \\ 0 & 0 & P^{\perp} \end{pmatrix} \tag{A25}$$
 where $P^{\parallel} = -2.70 \, \text{GPa}$, $P^{\perp} = -4.30 \, \text{GPa}$, and $P^{s} =$

where $P^{\parallel}=-2.70$ GPa, $P^{\perp}=-4.30$ GPa, and $P^{\rm s}=0.13$ GPa. The six eigenvalues of ω are the trivial 0, the doubly-degenerate -12λ , and the triply-degenerate -8λ . The contributions from the -12λ eigenmodes couple to $P^{\parallel}-P^{\perp}$ while the -8λ eigenmodes couple to $P^{\rm s}$. Because the second dipole contribution is more than order of magnitude smaller, it does not significantly change the peak loss temperature. Both terms contribute to \mathcal{L}' , while $\mathcal{L}^{\rm b}=0$. In order to identify the peak loss temperature for a single dominant eigenmode, we note that the maximum in Eqn. A20 occurs when $\nu=-r$. Writing $\lambda=\nu_0\exp(-E^{\rm ts}/k_{\rm B}T)$, we find that the peak loss temperature at

$$T_{\text{max loss}} = \frac{E^{\text{ts}}}{k_{\text{B}} \ln{(12\nu_0/\nu)}}.$$
 (A26)

For systems where P^s was significant compared with $P^{\parallel} - P^{\perp}$, the peak loss temperature equation would change. The computational results for the damping are available at Ref. [50].

J. Bednorz and K. Müller, Z. Phys. B Cond. Mat. 64, 189 (1986).

^[2] A. V. Barasheva and A. C. Arokiam, Phil. Mag. Lett. 86, 321 (2006).

^[3] T. Garnier, M. Nastar, P. Bellon, and D. R. Trinkle, Phys. Rev. B 88, 134201 (2013).

^[4] A. Barbu and A. Ardell, Scripta Metal. 9, 1233 (1975).

^[5] B. Masters, Solid State Commun. 9, 283 (1971).

^[6] G. Watkins, Phys. Rev. B 12, 4383 (1975).

^[7] M. Van Dijk, A. Burggraaf, A. Cormack, and C. Catlow, Solid State Ionics 17, 159 (1985).

^[8] D. O. Scanlon, N. M. Galea, B. J. Morgan, and G. W. Watson, J. Phys. Chem. C 113, 11095 (2009).

^[9] H. Höhler, N. Atodiresei, K. Schroeder, R. Zeller, and P. H. Dederichs, Phys. Rev. B 71, 035212 (2005).

^[10] M. Todorova, W. X. Li, M. V. Ganduglia-Pirovano, C. Stampfl, K. Reuter, and M. Scheffler, Phys. Rev. Lett. 89, 096103 (2002).

^[11] K. Reuter and M. Scheffler, Phys. Rev. Lett. 90, 046103 (2003).

^[12] C. Stampfl, M. V. Ganduglia-Pirovano, K. Reuter, and M. Scheffler, Surf. Sci. 500, 368 (2002).

^[13] J. Wöllenstein, M. Burgmair, G. Plescher, T. Sulima, J. Hildenbrand, H. Böttner, and I. Eisele, Sens. Actuator B-Chem. 93, 442 (2003).

^[14] Y. Okamoto, T. Imanaka, and S. Teranishi, J. Catal. 65, 448 (1980).

^[15] M. Hutchins, P. Wright, and P. Grebenik, Solar Energy Mater. 16, 113 (1987).

^[16] F. Švegl, B. Orel, M. Hutchins, and K. Kalcher, J. Electrochem. Soc. 143, 1532 (1996).

- [17] W. Koshibae, K. Tsutsui, and S. Maekawa, Phys. Rev. B 62, 6869 (2000).
- [18] S. Sun and C. Murray, J. Appl. Phys. 85, 4325 (1999).
- [19] T. Nishizawa and K. Ishida, J. Phase Equilib. 4, 387 (1983).
- [20] D. P. Dinega and M. Bawendi, Angew. Chem. Int. Ed. 38, 1788 (1999).
- [21] I. de PR Moreira, A. Roldán, F. Illas, et al., J. Chem. Phys. 133, 024701 (2010).
- [22] J. Snoek, Physica 8, 711 (1941).
- [23] P. E. Blöchl, Phys. Rev. B 50, 17953 (1994).
- [24] G. Kresse and D. Joubert, Phys. Rev. B 59, 1758 (1999).
- [25] G. Kresse and J. Hafner, Phys. Rev. B 47, 558 (1993).
- [26] G. Kresse and J. Hafner, Phys. Rev. B 49, 14251 (1994).
- [27] G. Kresse and J. Furthmüller, Comput. Mater. Sci. 6, 15 (1996).
- [28] G. Kresse and J. Furthmüller, Phys. Rev. B **54**, 11169 (1996).
- [29] J. P. Perdew, K. Burke, and M. Ernzerhof, Phys. Rev. Lett. 77, 3865 (1996).
- [30] H. J. Monkhorst and J. D. Pack, Phys. Rev. B 13, 5188 (1976).
- [31] H. Jónsson, G. Mills, and K. W. Jacobsen, in *Classical and quantum dynamics in condensed phase simulations*, edited by B. J. Berne, G. Ciccotti, and D. F. Coker (World Scientific, 1998) pp. 385–404.
- [32] G. Henkelman, B. P. Uberuaga, and H. Jónsson, J. Chem. Phys. 113, 9901 (2000).
- [33] M. S. Blanter, I. S. Golovin, H. Neuhauser, and H.-R. Sinning, Internal Friction in Metallic Materials (Springer, 2007).

- [34] P. Schiller, Il Nuovo Cimento 33B, 226 (1976).
- [35] M. Weller, G. Haneczok, and J. Diehl, Phys. Stat. Sol. (b) 172, 145 (1992).
- [36] J. N. Pratt, W. J. Bratina, and B. Chalmers, Acta Metall. 2, 203 (1954).
- [37] D. Gupta and S. Weinig, Acta Metall. 10, 292 (1962).
- [38] E. Bisogni, G. Mah, and C. Tvert, J. Less Common Metals **7**, 197 (1964).
- [39] K. M. Browne, Scripta Metall. 5, 519 (1971).
- [40] K. M. Browne, Acta Metall. 20, 507 (1972).
- [41] F. Povolo and E. A. Bisogni, Acta Metall. 14, 711 (1966).
- [42] J.-E. Bidaux, R. Schaller, and W. Benoit, Acta Metall. 37, 803 (1989).
- [43] D. R. Trinkle, Philos. Mag. 96, 2714 (2016).
- [44] G. H. Vineyard, J. Phys. Chem. Solids 3, 121 (1957).
- [45] Y. Hanlumyuang, P. Gordon, T. Neeraj, and D. Chrzan, Acta mater. 58, 5481 (2010).
- [46] C. Varvenne, F. Bruneval, M.-C. Marinica, and E. Clouet, Phys. Rev. B 88, 134102 (2013).
- [47] T. Garnier, V. R. Manga, P. Bellon, and D. R. Trinkle, Phys. Rev. B 90, 024306 (2014).
- [48] H. Kim and D. R. Trinkle, Comp. Mater. Sci. 119, 41 (2016).
- [49] R. G. A. Veiga, M. Perez, C. Becquart, E. Clouet, and C. Domain, Acta mater. 59, 6963 (2011).
- [50] D. R. Trinkle, "Onsager," http://dallastrinkle.github.io/Onsager (2019).